Comparisons between numerical and experimental data for the planar rocking-block dynamics– Part I: free-rocking

Hongjian Zhang[*], Bernard Brogliato[†], Caishan Liu[‡]

May 3, 2011

Abstract

This paper concerns the dynamics of planar rocking blocks, which are mechanical systems subject to two unilateral constraints with friction. A recently introduced multiple impact law that incorporates Coulomb friction is validated through numerous comparisons between numerical simulations and experimental data obtained elsewhere by other authors. They concern the free-rocking motion with no base excitation. The comparisons demonstrate that the proposed impact model allows one to correctly predict the block's motions. Especially the free-rocking experiments can be used to fit the impact law parameters (restitution and friction coefficients, width). The free-rocking fitted parameters are then used in the excited-base cases (see Part II).

Keywords: rocking block, multiple impacts, Coulomb friction, free-rocking.

1 Introduction

Modeling the dynamics of a rigid block hitting a rigid ground has attracted the attention of scientists in the field of Earthquake Engineering for a long time, see *e.g.* [2, 10, 12, 19, 22, 23, 26, 30, 31, 32, 34, 35] to cite a few. In parallel the field of impact dynamics has witnessed an intense activity in the past twenty-five years, see *e.g.* [5, 7, 9, 29] and references therein. It happens that the problem of modeling impacts with friction is a tough issue, especially when there are several simultaneous contact points (multiple impacts with friction). Typically the so-called *rocking block* problem involves double-impacts with friction, when one assumes that the base contacts the ground at two points only. Together with chains of balls, the rocking block is an apparently simple multibody system (the block and the ground), however it involves multiple impacts with friction and its modeling is consequently not simple at all.

In [3] experimental tests were led and compared to the model with Housner angular restitution r [10] calculated from the conservation of angular momentum before and after the shock. It was found that the analytical value of $r = -\frac{2l^2-L^2}{2L^2+2l^2}$, where l and L are the block height and width respectively, in [3] did not match with the experimental one. Similar conclusions were drawn in [21] who found a rather big discrepancy between the analytical and the experimental values of r. Usually the experimentally measured values for r are larger than the theoretically predicted ones, and many authors simply fit r with the data without questioning the model [3, 12, 21, 27, 31].

[*]State Key Laboratory for Turbulence and Complex Systems, College of Engineering, Peking University, Beijing 100871, People's Republic of China. Work performed while at INRIA, BIPOP project-team, ZIRST Montbonnot, 655 avenue de l'Europe, 38334 Saint Ismier, France, e-mail: hongjian.zhang@inrialpes.fr, zhanghj@pku.edu.cn; Funded by China Scholarship Council No. 2009601276 and by ANR project Multiple Impact ANR-08-BLAN-0321-01.

[†]INRIA, BIPOP project-team, ZIRST Montbonnot, 655 avenue de l'Europe, 38334 Saint Ismier, France, e-mail: Bernard.Brogliato@inrialpes.fr

[‡]State Key Laboratory for Turbulence and Complex Systems, College of Engineering, Peking University, Beijing 100871, People's Republic of China, e-mail: liucs@pku.edu.cn

Recently experimental tests on concrete blocks have shown [8] that the ratio between the measured r and the above one may be smaller or larger than one, despite it is usually smaller (see Table II in [8]), contradicting the older conclusions. These authors also showed the unability of the kinematic angular restitution law to predict the free-rocking motion (see figure 18 in [8]). Lispcombe et al. [12] calculated r by introducing the kinematic restitution and adding constraints for no slipping or unidirectional slip. Yilmaz et al. [34] used a generalization of Routh's approach and so-called impulse correlation ratios, without friction. They found good agreements between their simulations and their experiments. Pena, Prieto et al. [19, 20, 22] performed lots of experiments and also proposed a new model for rocking. It is noteworthy that in their experiments Pena et al. [19] found better matching between the above value of r and the experimental values, which differ by much smaller percentage than in [3, 21]. The fact that a block rotating around one corner and impacting at the other corner may rebound at both corners (and thus become airborne) is studied in [12]. Some authors like Palmeri et al. [18] introduced some compliance at the contacts and frictional effects in order to cope with such complex dynamics. In [2] the nonsmooth mechanics framework is adopted and friction with a non-constant sliding coefficient is used. In [23] the normal and tangential (Coulomb's friction) models are penalized so that the rocking block (sticking rocking) dynamics is a smooth second order differential equation, that may be stiff. Taniguchi [30] uses the Housner angular velocity restitution coefficient, and Coulomb's law during non-impacting phases of motion. He points out that perfect rocking seldom occurs, whereas stick/slip phases may be the common behaviour.

The conclusions to be drawn from all these works are that experimental results are not always easy to interpret. It happens that the dynamics of a block on a rigid ground with friction is a rather unexpectedly complex process. Also, the experiments are always prone to a number of uncertainties like: friction with grooves on the foundation, vibrational effects inside the block, which are not well understood, deformations and vibrations of the foundation, heterogeneous material so that the center of mass is not the geometric center, damage at the contact points, so that the corners are not the exact rotation points, three-dimensional effects, pivot friction at the contact points, line or surface contact effects, *etc*. By line or surface contact effects, we mean that the block's surface that collides with the ground, and the ground itself, never possess a perfect geometry. It may happen that the contact is established at some isolated points of the surface, or with some subsets of the surface. Thus the block's geometric width may not correspond to its "ideal rocking block" equivalent width, or *effective* width. The two extreme cases are when the base is concave (the corners are the contact/impact points and the geometric and effective width are equal), and when it is convex (there are no more impacts). Such issues where raised in [24] where it is noted that *overturning responses of blocks with multiple rocking points are equivalent to more slender blocks with simple basal contact conditions*. In other words, when the contact occurs at several points of the base, the equivalent perfect block with two contact/impact points at A and B is more slender. In addition it has been noticed experimentally that the block's motion may be very sensitive to initial data, a vey small change in the initial position can cause a big change in the block's response [3, 17]. For all these reasons, getting very accurate prediction with rigid body models is expected to be a tough task in general. Getting general tendencies may be a reasonable and useful goal, instead. It is known that stick/slip behaviour during the impacts may influence significantly the shock dynamics [29]. It is apparent from the above results and comments that introducing a correct model of friction in the block dynamics, *both* at impacts and during contact phases, is a mandatory step. Tackling this objective within the framework of rigid body systems and multiple impacts with friction is done in the sequel of this paper, and in Part II.

The objective of Part I is to demonstrate that the LZB multiple impact model introduced in [13, 14, 15, 16, 39], is quite suitable to model the free-rocking motion (the base is fixed, the blocks are initialized with zero velocity and a non zero tilt, one corner in contact with the base). This is shown through detailed comparisons between numerical results obtained with the LZB model (the event-driven code used for the simulations is available in [36]), and experimental results obtained in Pena et al [19, 20] and Lipscombe et al [12]. Further comparisons with the experimental results in [8] are reported in [36]. Those comparisons concern free-rocking (fixed base), the onset of rocking and the onset of overturning (with horizontal base excitation) being the subject of Part II [38]. Our results are both qualitative (*i.e.* they concern general properties or tendencies), and quantitative when this has been possible (in the case of the experiments reported in [19, 20], all the experimental data and figures were made available to us, making possible accurate comparisons between the numerical and the experimental figures). The conclusions are quite positive and confirm the results obtained in [14, 16, 39] where detailed comparisons with experimental data for Newton's cradle [16], bouncing dimer [39], column of beads [14], are made: the LZB model does encapsulate the main dynamical effects of multiple impacts with Coulomb friction. It is noteworthy that our model seems to be able to predict the motion for systems ranging from few grams (the dimer [39]) to several hundreds of kilograms (the rocking blocks in [19, 20]). Most importantly it is shown in Part II that the free-rocking experiments can be used to fit the parameters (restitution coefficients, friction coefficients, widthes) which are used to predict more complex motions with base excitation. The paper is organized as follows: in section 2 the planar block dynamics and the multiple impact model are introduced. Section 3 is dedicated to the comparisons between the experimental data in [20], [12] and numerical results, for free-rocking motion. Conclusions end the paper in section 4.

2 The block dynamics and the impact law

2.1 The block dynamics outside the collisions

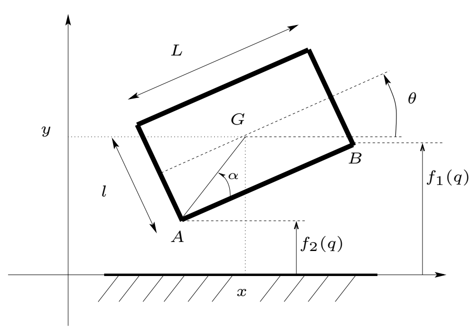

Figure 1: The block.

Let us consider the block as a three degrees of freedom planar homegeneous solid, with generalized coordinates $q^T = (x, y, \theta)$, where x and y are the horizontal and vertical positions of the center of gravity, θ is the angular position, see figure 1. Following [5, Chapter 6] we infer that the block, when $y \leq \sqrt{l^2 + L^2}$, is subject to two unilateral constraints:

$$\left\{\begin{array}{l} f_1(q) = y - \frac{l}{2}\cos(\theta) + \frac{L}{2}\sin(\theta) \geq 0 \\ \\ f_2(q) = y - \frac{l}{2}\cos(\theta) - \frac{L}{2}\sin(\theta) \geq 0, \end{array}\right. \tag{1}$$

where $f_1(q) \geq 0$ expresses that point B cannot penetrate into the ground, while $f_2(q) \geq 0$ expresses the same for point A. The underlying assumption is that the block/ground contact can be represented by the two points A and B at the corners. The dynamics of the block subject to (1) and Coulomb friction is given by:

$$
\begin{cases}
m\ddot{x}(t) & = \lambda_{t,1}(t) + \lambda_{t,2}(t) \\
m\ddot{y}(t) & = \lambda_{n,1}(t) + \lambda_{n,2}(t) - mg \\
I_G\ddot{\theta}(t) & = \lambda_{n,1}(t)\left(\frac{l}{2}\sin(\theta(t)) + \frac{L}{2}\cos(\theta(t))\right) + \lambda_{n,2}(t)\left(\frac{l}{2}\sin(\theta(t)) - \frac{L}{2}\cos(\theta(t))\right) \\
& \quad + \left(\frac{l}{2}\cos(\theta) - \frac{L}{2}\sin(\theta)\right)\lambda_{t,1} + \left(\frac{l}{2}\cos(\theta) + \frac{L}{2}\sin(\theta)\right)\lambda_{t,2} \\
& \\
& 0 \le \lambda_n(t) \perp f(q(t)) \ge 0 \\
& \lambda_{t,i}(t) \in -\mu_i\lambda_{n,i}(t)\,\mathrm{sgn}(v_{t,i}(t)), i = 1, 2
\end{cases}
\tag{2}
$$

where $\mu_i > 0$ is the friction coefficient at contact i, and $v_{t,i}$ is the tangential velocity at the point i, *i.e.* $v_{t,1} = \dot{x} + \left(\frac{l}{2}\cos(\theta) + \frac{L}{2}\sin(\theta)\right)\dot{\theta}$ at B and $v_{t,2} = \dot{x} + \left(\frac{l}{2}\cos(\theta) - \frac{L}{2}\sin(\theta)\right)\dot{\theta}$ at A (from which $v_{t,1} = v_{t,2}$ when $\theta = 0$). Notice that if the contact point i detaches then the complementarity conditions imply that $\lambda_{n,i} = 0$ so $\lambda_{t,i} = 0$. The dynamics in (2) stands for fixed ground. The complementarity conditions are componentwise, $f(q)^T = (f_1(q), f_2(q))$, $\lambda_n^T = (\lambda_{n,1}, \lambda_{n,2})$. For a block with G at the geometric center one has $I_G = \frac{m}{12}(l^2 + L^2)$. In (2) we have not yet considered the impacts with the ground, but only those phases of motion where the contact force is a bounded function of time. From (1) and (2) the Linear Complementarity Problem (LCP) that allows one to calculate the contact forces during the smooth phases of motion (*i.e.* outside impacts) is given in the frictionless case by:

$$
0 \le \lambda_n(t) \perp \frac{d^2}{dt^2} f(q(t)) = A(\theta)\lambda_n(t) + B(\theta, \dot{\theta}) \ge 0 \tag{3}
$$

with $A(\theta) = \begin{pmatrix} \frac{1}{m} + \frac{1}{4I_G}(l\sin(\theta) + L\cos(\theta))^2 & \frac{1}{m} + \frac{1}{4I_G}(l^2\sin^2(\theta) - L^2\cos^2(\theta)) \\ \frac{1}{m} + \frac{1}{4I_G}(l^2\sin^2(\theta) - L^2\cos^2(\theta)) & \frac{1}{m} + \frac{1}{4I_G}(l\sin(\theta) - L\cos(\theta))^2 \end{pmatrix}$, $A(\theta) = A^T(\theta)$, $B(\theta, \dot{\theta}) = \begin{pmatrix} -g + \frac{1}{2}\dot{\theta}^2(l\cos(\theta) - L\sin(\theta)) \\ -g + \frac{1}{2}\dot{\theta}^2(l\cos(\theta) + L\sin(\theta)) \end{pmatrix}$. One calculates that $\det(A(\theta)) = \frac{L^2}{mI_G}\cos^2(\theta)$ so that $A(\theta)$ is positive definite except at $\theta = \pm\frac{\pi}{2}$. These values are however outside the range of block orientations within which the analysis is done. We conclude that for all angles $\theta \in (-\frac{\pi}{2}, \frac{\pi}{2})$ $A(\theta) > 0$ and the normal contact force λ_n can be computed uniquely in the frictionless case as the solution of the LCP in (3) whatever θ and $\dot{\theta}$. $A(\theta)$ is the so-called Delassus' matrix of the system (1) (2). When friction is considered the stick/slip behaviour introduces new modes during the contact phases. It is possible to rewrite compactly the smooth part of the dynamics in (2) as:

$$
M\ddot{q}(t) = W_n(q(t))\lambda_n(t) + W_T(q(t))\lambda_t(t) - \mathbf{g} \tag{4}
$$

with $\mathbf{g} = (0\ mg\ 0)^T$, $M =$diag(m, m, I_G), W_n and W_t are easily identified from (2). One has $v_n = W_n^T(q)\dot{q}$, $v_t = W_T^T(q)\dot{q}$, where $v_n = (v_{n,1}\ v_{n,2})^T$, $v_t = (v_{t,1}\ v_{t,2})^T$ denote the local velocities of the contact points [1]. Also $A(\theta) = W_n^T(q)M^{-1}W_n(q)$. The LCP (3) becomes if $\mu_i > 0$:

$$
0 \le \lambda_n(t) \perp A(\theta)\lambda_n(t) + W_n(q)M^{-1}W_T(q)\lambda_t(t) + B(\theta, \dot{\theta}) \ge 0 \tag{5}
$$

The details on how to analyze and solve such problems is outside the scope of this paper, see [1, 15]. Let us just mention that, in general, friction may create inconsistencies and indeterminacies [5, §5.5] yielding Painlevé paradoxes. We have never met such issues for the rocking block in all our simulations, and consequently do not insist on them.

Remark 1. *In this paper the basic Coulomb's law is enhanced to incorporate static and dynamic friction, see figure 2.*

2.2 The impact dynamics

The impact model proposed in [13, 14, 15, 16, 39] is summarized in this section, it will be named the LZB impact model in the following. The contact stiffnesses are denoted as k_i, the potential energy at contact i is E_i, η is the elasticity coefficient. The matrix W_n is the jacobian between the generalized velocities $\dot{q}$ and the contact points normal relative velocities, *i.e.* $W_n^T = \frac{\partial f}{\partial q} = \nabla f^T(q) \in \mathbb{R}^{2\times 3}$, whereas $W_n \lambda_n$ represents the generalized contact force associated to the generalized coordinates q, see (2) and (4). $P_{n,i}$ denotes the interaction normal force impulse at contact point i, $P_n = (P_{n,1}, P_{n,2})^T$ is the vector of normal impulses. The mass matrix $M \in \mathbb{R}^{3\times 3}$ is given by $M = \text{diag}(m, m, I_G)$. An important assumption in this model, that is an extension of the Darboux-Keller approach [5], is that positions q are constant during the impact process. Thus $W_n(q)$ is constant during the collision process. In the frictionless case one obtains:

- Contact parameters: $\gamma_{ij} = \frac{k_i}{k_j}$ (stiffnesses ratios), $e^*_{n,j}$ (energetic restitution coefficients), $1 \le i \le 2$, $1 \le j \le 2$, η ($= 1$ for linear elasticity, $= \frac{3}{2}$ for Hertz contact, or other values).
- Dynamical equation:

$$M \frac{d\dot{q}}{dP_{n,i}} = W_n \frac{dP_n}{dP_{n,i}} \ \text{ if } \ E_{ji}(P_{n,j}, P_{n,i}) \le 1 \ \text{ for } j \ne i \tag{6}$$

with the distributing law[1]:

$$\frac{dP_{n,j}}{dP_{n,i}} = \gamma_{ji}^{\frac{1}{\eta+1}} \left(E_{ji}(P_{n,j}, P_{n,i})\right)^{\frac{\eta}{\eta+1}}, \tag{7}$$

and the potential energies ratios:

$$E_{ji} = \frac{E_j(P_{n,j})}{E_i(P_{n,i})}, \ \ 1 \le i \le 2, \ 1 \le j \le 2, \tag{8}$$

where:

$$E_j(P_{n,j}) = \int_0^{P_{n,j}(t)} \mathbf{w}_j^T \dot{q} dP_{n,j}. \tag{9}$$

The time t_c of maximal compression at the contact j is calculated from $\dot{\delta}_j(t_c) = 0$ where δ_j is the relative normal displacement at contact j ($\dot{\delta} = W_n \dot{q} = \nabla f^T(q)\dot{q}$). The termination time t_f is calculated from the energy constraint $W_{r,j} = -(e^*_{n,j})^2 W_{c,j}$, where the works during expansion and compression phases are given by:

$$W_{r,j} = \int_0^{P_{n,j}(t_c)} \mathbf{w}_j^T \dot{q} dP_{n,j}, \ \ W_{c,j} = \int_{P_{n,j}(t_c)}^{P_j(t_f)} \mathbf{w}_j^T \dot{q} dP_{n,j}. \tag{10}$$

The vectors $\mathbf{w}_j = \nabla f_j(q)$ are the columns of the jacobian matrix W_n. The impulse $P_{n,i}$ at contact i is the so-called principal impulse that is chosen as the new time-variable in the impact model. It may change during the impact process, see [13] for details. In view of (2) in the frictionless case the impact dynamics reduce to a two-dimensional system because $\frac{d\dot{x}}{dP_{n,i}} = 0$. Coulomb's friction can be easily added in the impact model, at the force (or infinitesimal impulse) level. In such a case the right-hand-side of (6) has to be modified accordingly with the insertion of the tangential force components, see (2) and (4):

$$M \frac{d\dot{q}}{dP_{n,i}} = W_n \frac{dP_n}{dP_{n,i}} + W_t \frac{dP_t}{dP_{n,i}} \ \text{ if } \ E_{ji}(P_{n,j}, P_{n,i}) \le 1 \ \text{ for } j \ne i \tag{11}$$

In this work we use an enhanced model of friction with a static μ_s and a dynamic μ friction coefficients, see figure 2. The same model is used outside and during the impacts (where it is written at the infinitesimal impulse level). This impact model is therefore a rigid body model that

[1] The power of the potential energies ratio $E_{ji}(P_{n,j}, P_{n,i})$ is inverted in [13, 14].

incorporates some flexibility effects through the distributing law, with one restitution coefficient and one (or two) friction coefficient *per* contact. More details on the implementation may be found in [13, 15, 16], and the code which has been used for the simulations is given in [36] (a similar event-driven code is also available in the SICONOS platform[2]). For the dynamics outside the impacts, in the frictionless case the LCP in (3) is used to integrate the system, and either an explicit Euler or a Runge-Kutta algorithms are implemented. When Coulomb friction is present the scheme is the same as the one used in [39] and described in [15]. It is noteworthy that the numerical scheme that is employed next is of the *event driven* type (see [1] for a description), and that all the stick/slip and contact/detachment conditions are carefully taken care of (taking care, in particular, of the multivalued feature of the friction law at zero tangential velocity). Two flowcharts of the event-driven method are depicted in Part II (see figures 15 and 16 in [38]). To summarize we use an event-driven method with the complementarity model (2) outside impacts and the above LZB impact dynamics when an impact is detected. Two flowcharts of the code are provided in Part II [38].

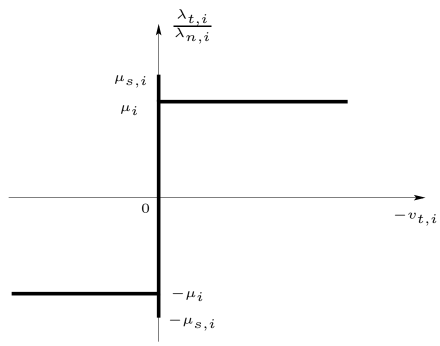

Figure 2: The friction model.

Remark 2. *An interesting feature of the LZB impact law is that it allows for stick/slip transitions* during *the impacts, as shown in [37]. This means that the relative tangential velocity can reverse its sign during the collision without implying energetical incoherencies, as it is the case with kinematic restitution laws [7]. Tangential velocity reversals do occur in the planar block, see figure 21 (b) in [36]. Notice that complementarity modeling has been introduced for block/ground systems in [2].*

3 Comparisons with free-rocking experimental data

In this section it is proved that the LZB model can be fitted well to provide correct predictions of free-rocking motions, with fixed base. Free-rocking corresponds to the block initialized with a non-zero angle $\theta(0)$, one corner in contact, and zero initial velocity $\dot{\theta}$. Two different sets of experimental results are used, from [20] and [12]. The comparisons with the data in [19, 20] are done from the accurate experimental data (not available in the papers but provided to us by the authors), whereas those with the data in [12] are made only from the figures available in the papers and are therefore less accurate and more qualitative.

3.1 Comparisons with the experimental data in Pena et al [20]

Experimental data led on blue granite stone blocks are reported in [20]. In this section we provide detailed comparisons between the numerical simulations obtained with the LZB model and the

[2]http://siconos.gforge.inria.fr/

experimental data of [20][3] The tests concern four specimens of blocks with ratios $\frac{l}{L} \approx \frac{1}{0.25} = 4$ and thickness $d = 0.754$m (specimen 1), $\frac{l}{L} \approx \frac{1}{0.17} = 5.88$ and thickness $d = 0.502$m, (specimen 2), $\frac{l}{L} \approx \frac{1}{0.12} = 8.33$ and thickness $d = 0.375$m (specimen 3), $\frac{l}{L} \approx \frac{0.457}{0.16} = 2.85$ and thickness $d = 0.750$m (specimen 4), where l and L are in meters. Specimen 3 is the most slender one with the smallest thickness, and is of the *tower* type. Specimen 4 is the less slender one with the largest thickness and is of the *slice* type. The masses of the blocks are estimated from their dimensions and density, and are given by 503 kg, 228 kg, 120 kg, 245 kg for specimens 1, 2, 3, 4 respectively.

3.1.1 The $\theta(t)$ response

Let us study the $\theta(t)$ response of the blocks. The results are depicted in figures 3, 4, 6 (a), 6 (b), and 7. The corresponding responses $y_A(t)$ and $y_B(t)$ are in figures 5 (a) and 5 (b). The fitted restitution coefficients are $e^*_{n,i} = 0.999$ for specimen 2 in figure 4, and $e^*_{n,i} = 0.97$ for the first 10 impacts and $e^*_{n,i} = 0.88$ for the last impacts, for specimen 1 in figure 3. For specimen 4 the fitted values are $e^*_{n,i} = 0.99$ for the first 4 impacts, $e^*_{n,i} = 0.84$ between impact 5 and impact 8, and $e^*_{n,i} = 0.99$ for the last impacts (see comment (ii) in section 3.1.3 for explanations about this switching parameter). The fitted dimensions are $\frac{l}{L} = \frac{1}{0.23} \approx 4.35$ for specimen 1 and $\frac{l}{L} = \frac{1}{0.155} = 6.45$ for specimen 2, $\frac{l}{L} = \frac{0.457}{0.10} = 4.57$ for specimen 4. The friction coefficients are chosen as $\mu = 0.3$ and $\mu_s = 0.577$ as in [20]. The results for specimen 3 are depicted in figures 6 (a) and 6 (b). In figure 6 (a) the magnitudes of the oscillations are correctly predicted with the same restitution as for the fitted values of specimens 1 and 2, *i.e* $e^*_{n,i} = 0.999$, however there is a shift in the oscillations pseudo-period. The parameters are varied in figure 6 (b) with a smaller restitution coefficient and width, but this does not change much the result (see the comments about three-dimensional effects below). The results for specimen 4 are in figure 7. As indicated above in this case we had to switch e^*_n twice to obtain a good matching. In Tables 2 to 7 are reported some data on the impact times and the maximal amplitudes that correspond to the $\theta(t)$ responses for specimens 1, 2 and 4. All these results show that the LZB model has very good prediction capabilities. The large errors in Table 7 are due to some imperfect measurement data at the peaks and should not be considered as significant results. Such issues are common in experimental data and do not call into question neither the experimental data from [19, 20] nor our comparison results.

Uncertainties in e^*_n It happens that the rocking motion is highly sensitive to parameters variations, which renders the calibration of the parameters a delicate process. In figure 8 (a) is depicted the $\theta(t)$ response for specimen 2, with $e^*_{n,i} = 0.95$, which represents a variation of 4.9% with respect to the fitted value $e^*_{n,i} = 0.999$ in figure 4. The same is done in figure 8 (b) with $e^*_{n,i} = 0.99$, which represents a variation of 1% with respect to the fitted value. It is apparent that a very small variation on $e^*_{n,i}$ produces a large mismatch in the $\theta(t)$ response.

Uncertainties in the width L The sensitivity of the $\theta(t)$ response w.r.t. variations in $\frac{l}{L}$ is shown in figure 9 (a) for specimen 2, and in figure 9 (b) for specimen 4. The values for $e^*_{n,i}$ are the fitted ones. It follows that the uncertainty in the width L affects mainly the pseudo frequency of the oscillations and has little effect on the magnitudes. This is in contrast with uncertainties on $e^*_{n,i}$ which affect both the frequency and the magnitude, see figure 8 (a). The various widthes which enter the study are recapitulated in Table 1. The geometric widthes are those measured on the blocks. The experimental widthes are obtained from an estimation process using the Housner model, see section 4.1 in [19]. The other two sets of widthes are obtained by the fitting the parameters. The choices for smaller widthes in simulation are in agreement with the conclusion in [24], where what we call the width in simulation may be called the effective width following [24].

[3]All the data corresponding to the comparisons presented in this section have been made available to us by Dr F. Pena from UNAM, Mexico.

	1	2	3	4
Geometric width	0.24	0.16	0.11	0.15
Experimental width	0.2394	0.1645	0.1552	0.1255
Width in simulations of [20]	0.2468	0.1696	0.1196	0.1464
Width in LZB model	0.23	0.155	0.12 and 0.115	0.10

Table 1: The various widthes.

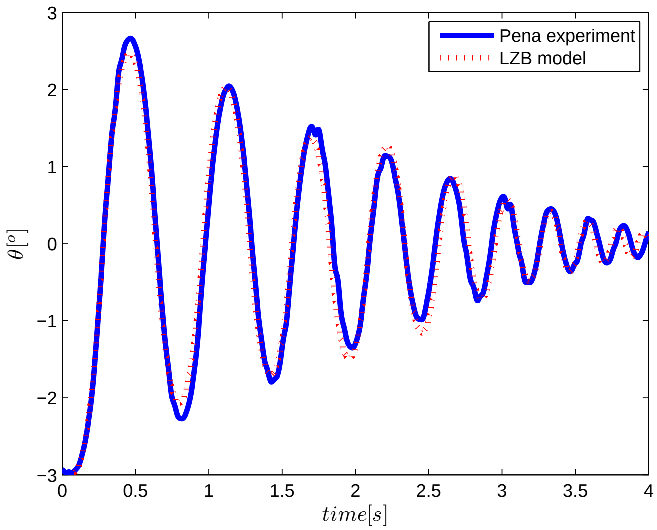

Figure 3: Numerical vs experimental values of $\theta(t)$, specimen 1. $e_n^* = 0.97$ and 0.88, $l = 1$m, $L = 0.23$m.

In short, due to the contact line geometry imperfections, the equivalent width of the model with two contact points must be smaller than the geometrical width of the real block.

The elasticity coefficient η The elasticity coefficient enters the LZB impact model through the co-called distributing law and the potential energies ratios $E_{ji}(P_j, P_i)$. In all the simulations of this Part and of Part II, we have made the choice $\eta = \frac{3}{2}$ (Hertz contact).

3-dimensional effects For specimen 3 the numerical results do not perfectly match with the experimental ones, see figures 6 (a) and 6 (b). This is due to 3-dimensional effects which occur for this block in the experiments as noted in [20]. This is why two values are indicated in Table 1 for specimen 3, because we were not able to fit the parameters.

3.1.2 The angular velocity restitution coefficient

The angular velocity restitution coefficient $r = \frac{\dot{\theta}(t^+)}{\dot{\theta}(t^-)}$ is widely used in the rocking block literature, and is known to be of limited applicability as recalled in the introduction. It is interesting to study its value from the numerical results that fit well with the experimental ones. Let us start with Table 3 in [20] where experimentally measured values of a kinematic angular restitution coefficient, denoted as μ in [20] and next as r_{exp} to avoid confusions, are reported from the free-rocking of the above four specimens of blocks. In [20] r_{exp} is computed indirectly from the averaged values of the expressions:

Impact no	Experiment IT (s)	Numerical IT (s)	Absolute error	Relative error in %
1	0.279	0.279	0	0
2	0.647	0.637	0.01	1.5
3	0.977	0.958	0.019	1.94
4	1.293	1.278	0.015	1.16
5	1.578	1.567	0.011	0.70
6	1.855	1.825	0.03	1.62
7	2.097	2.092	0.005	0.24
8	2.336	2.334	0.002	0.09
9	2.570	2.545	0.025	0.97
10	2.745	2.770	0.025	0.97
11	2.928	2.956	0.028	0.96
12	3.104	3.114	0.01	0.32
13	3.256	3.262	0.006	0.18
14	3.406	3.399	0.007	0.20
15	3.538	3.526	0.012	0.34
16	3.665	3.641	0.024	0.65

Table 2: The data of figure 3, specimen 1, impact times (IT).

Peak no	Experiment MA	Numerical MA	absolute error	Relative error in %
1	-2.968	-2.968	0	0
2	2.666	2.472	0.194	7.28
3	-2.271	-2.076	0.195	8.59
4	2.045	2.032	0.013	0.64
5	-1.794	-1.711	0.083	4.63
6	1.521	1.381	0.14	9.21
7	-1.352	-1.497	0.145	10.72
8	1.267	1.142	0.125	9.87
9	-0.986	-1.158	0.172	17.44
10	0.846	0.885	0.039	4.6
11	-0.738	-0.716	0.022	2.98
12	0.613	0.575	0.038	6.20
13	-0.504	-0.491	0.013	2.58
14	0.452	0.419	0.033	7.30
15	-0.363	-0.358	0.005	1.38
16	0.325	0.297	0.028	8.62

Table 3: The data of figure 3, specimen 1, maximum amplitudes (MA).

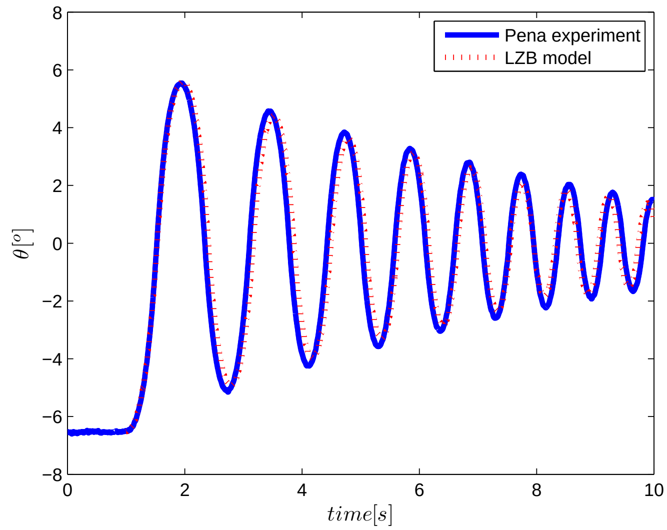

Figure 4: Numerical vs experimental values of $\theta(t)$, specimen 2. $e_n^* = 0.999$, $l = 1$m, $L = 0.155$m.

Impact no	Experiment IT (s)	Numerical IT (s)	Absolute error	Relative error in %
1	1.525	1.531	-0.006	0.39
2	2.347	2.442	-0.095	4.05
3	3.108	3.171	-0.063	2.03
4	3.785	3.861	-0.076	2.01
5	4.431	4.493	-0.062	1.40
6	5.019	5.082	-0.063	1.26
7	5.585	5.632	-0.047	0.84
8	6.105	6.158	-0.053	0.87
9	6.605	6.657	-0.052	0.79
10	7.075	7.119	-0.044	0.62
11	7.525	7.555	-0.03	0.40
12	7.952	7.947	0.005	0.06
13	8.362	8.323	0.039	0.47
14	8.745	8.695	0.05	0.57
15	9.123	9.061	0.062	0.68
16	9.477	9.408	0.069	0.73

Table 4: The data of figure 4, specimen 2, impact times (IT).

Peak no	Experiment MA	Numerical MA	absolute error	Relative error in %
1	-6.516	-6.520	-0.004	0.06
2	5.582	5.542	0.04	0.72
3	-5.152	-4.925	0.227	4.41
4	4.574	4.404	0.17	3.72
5	-4.241	-3.962	0.279	6.58
6	3.846	3.626	0.22	5.72
7	-3.574	-3.299	0.275	7.69
8	3.280	3.111	0.169	5.15
9	-3.046	-2.843	0.203	6.66
10	2.801	2.605	0.196	7.00
11	-2.593	-2.342	0.251	9.68
12	2.384	2.013	0.371	15.56
13	-2.237	-1.825	0.412	18.42
14	2.031	1.841	0.19	9.35
15	-1.926	-1.768	0.158	8.20
16	1.758	1.631	0.127	7.22

Table 5: The data of figure 4, specimen 2, maximum amplitudes (MA).

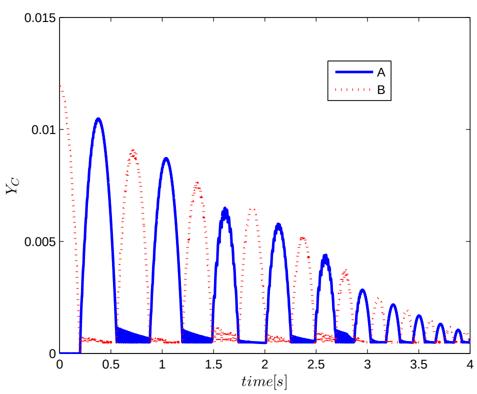

(a) Specimen 1, $C = A$ or $C = B$

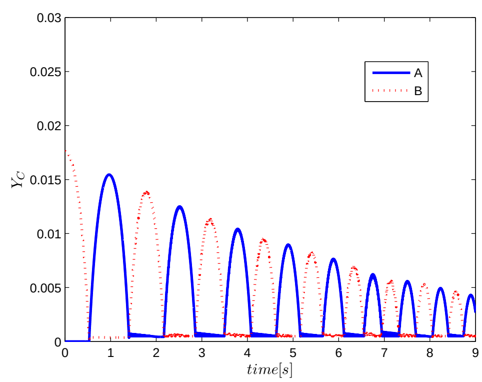

(b) Specimen 2, $C = A$ or $C = B$

Figure 5: Numerical values of $y_C(t)$.

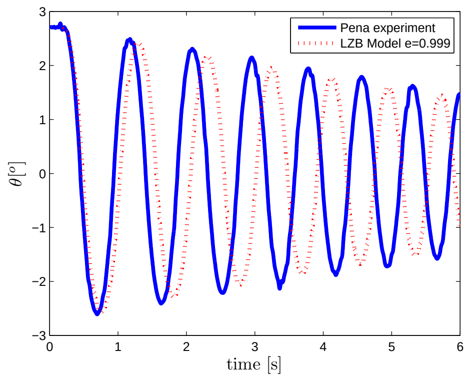

(a) $e^*_{n,i} = 0.999$, $l = 1$m, $L = 0.12$m.

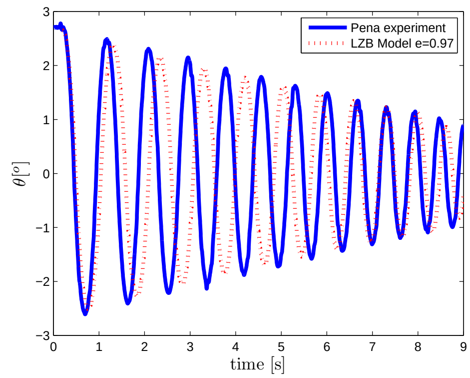

(b) $e^*_{n,i} = 0.97$, $l = 1$m, $L = 0.115$m.

Figure 6: Numerical vs experimental values of $\theta(t)$, specimen 3

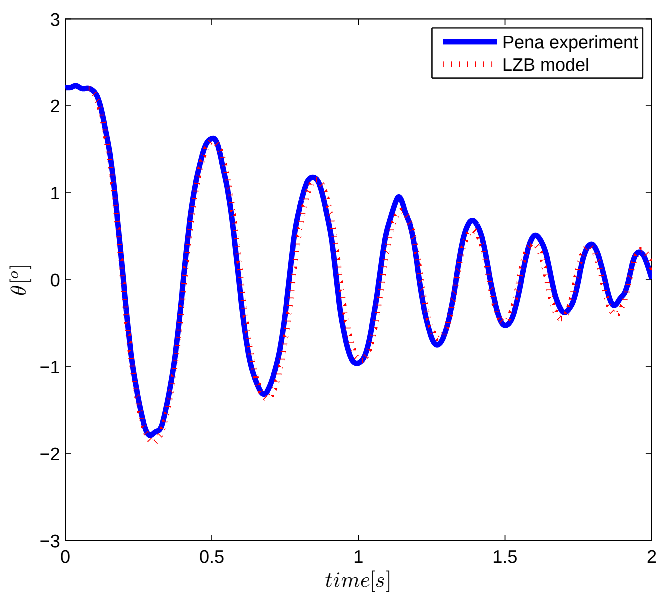

Figure 7: Numerical vs experimental values of $\theta(t)$, specimen 4, $e^*_{n,i} = 0.99$, and 0.84, $l = 0.457$m, $L = 0.10$m.

Impact no	Experiment IT (s)	Numerical IT (s)	Absolute error	Relative error in %
1	0.199s	0.195s	0.004	2.01
2	0.403	0.406	-0.003	0.74
3	0.592	0.599	0.007	1.18
4	0.764	0.776	-0.012	1.55
5	0.925	0.937	-0.012	1.30
6	1.070	1.081	-0.011	1.03
7	1.208	1.213	-0.005	0.41
8	1.333	1.335	-0.002	0.15
9	1.449	1.446	0.003	0.21
10	1.556	1.548	0.008	0.51
11	1.659	1.643	0.016	0.96
12	1.751	1.741	0.01	0.57
13	1.841	1.831	0.01	0.54
14	1.921	1.924	-0.003	0.16

Table 6: The data of figure 7, specimen 4, impact times (IT).

Peak no	Experiment MA	Numerical MA	absolute error	Relative error in %
1	2.201	2.200	0.001	0.04
2	-1.789	-1.869	-0.08	4.47
3	1.626	1.594	0.032	1.97
4	-1.315	-1.363	-0.048	3.65
5	1.178	1.155	0.023	1.95
6	-0.962	-0.932	0.03	3.12
7	0.953	0.794	0.159	16.68
8	-0.749	-0.675	0.074	9.88
9	0.682	0.572	0.11	16.13
10	-0.525	-0.485	0.04	7.62
11	0.512	0.421	0.091	17.77
12	-0.376	-0.447	-0.071	18.88
13	0.408	0.385	0.023	5.63
14	-0.295	-0.399	-0.104	35.25

Table 7: The data of figure 7, specimen 4, maximum amplitudes (MA).

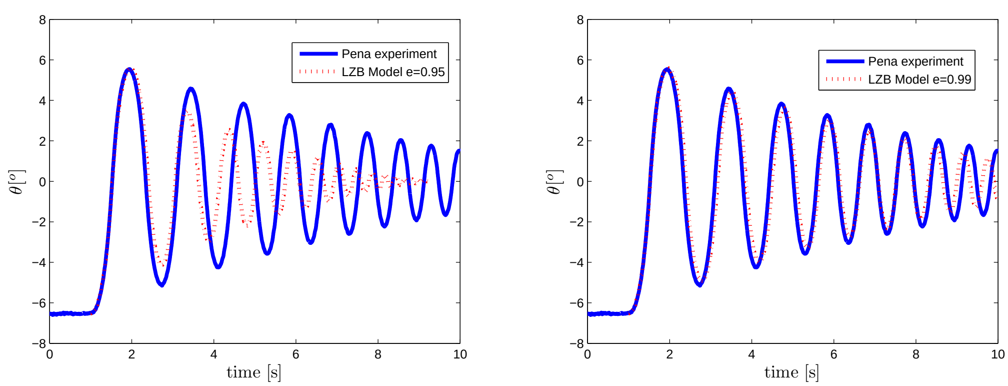

(a) $e^*_{n,i} = 0.95$

(b) $e^*_{n,i} = 0.99$

Figure 8: Sensitivity of the $\theta(t)$ response w.r.t. variations in $e^*_{n,i}$ (specimen 2).

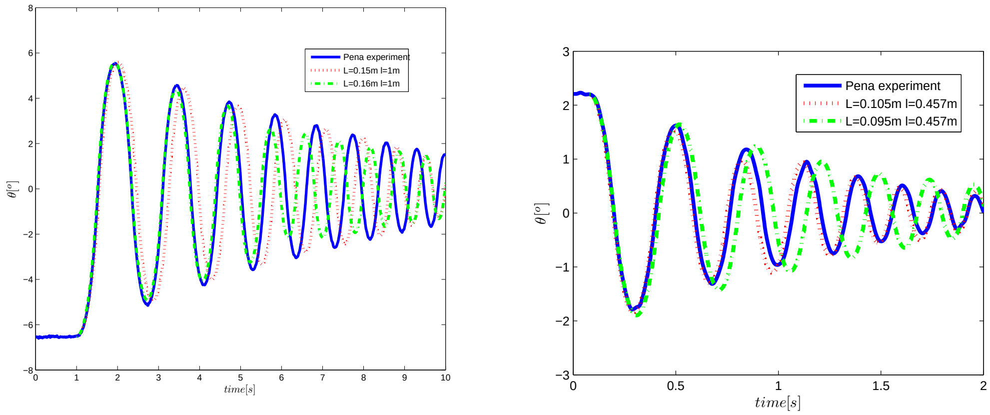

(a) Specimen 2 (b) Specimen 4

Figure 9: Sensitivity of the $\theta(t)$ response w.r.t. variations in L.

$$\left(\frac{\cos(\alpha - a_n) - \cos(\alpha)}{\cos(\alpha - a_0) - \cos(\alpha)}\right)^{\frac{1}{2n}} \tag{12}$$

where the a_n are the magnitudes of the block's orientation $\theta(t)$, n is the impact number. This expression is deduced from the energy at the nth impact as a function of the initial energy and r. This is also used in [8] to compute the energy of various rocking blocks (figures 15, 16, 17 in [8]). We shall use this way of computing r in figures 10 (a) and 11 (a). The angular restitution r is calculated directly from the ratios $\frac{\dot{\theta}(t^+)}{\dot{\theta}(t^-)}$ in figures 10 (b) and 11 (b). The latter are not available from the experimental data, but only from our numerical simulations with the LZB model in the previous section. However since they are calculated with the fitted parameters the computed values should be close to the experimental ones.

The masses indicated in [20]: $m \approx 503, 228, 120$ kg respectively[4]. In figures 10 (a) and 11 (a) are depicted the values of r_{LZB} and r_{exp} with the fitted parameters[5]. It is seen that r is almost constant from one impact to the next. The fist values of r_{exp} and r_{LZB} may be smaller than the other ones: this is explained by the absence of a rebound phase after the first impact, see figure 5. In figures 10 (b) and 11 (b) are depicted the values of $-r = \frac{\dot{\theta}(t^+)}{\dot{\theta}(t^-)}$, which differ from those of figures 10 (a) and 11 (a) which are computed as in [20]: they are less "smooth", in the sense that r varies more with some peaks.

3.1.3 Comments

- (i) The values for e_n^* (0.999 or 0.99) are large values, since other works on single granite/granite impacts without friction report values of the restitution coefficient ≈ 0.86 [11]. However it is also known from many experimental results that the restitution coefficient usually tends to 1 when the initial relative velocity tends to zero, see *e.g.* [28]. In the presented results the normal relative velocity is very small (about 0.02 m/s). This may explain this high value for e_n^*. Recall that for specimen 2 the planar rocking assumption is well respected, where no three dimensional effects could be noticed experimentally in [20].

[4] The masses are estimated from the density and the dimensions in [20], hence prone to some uncertainties.

[5] We call the fitted parameters the parameters used in figures 3, 4 and 7

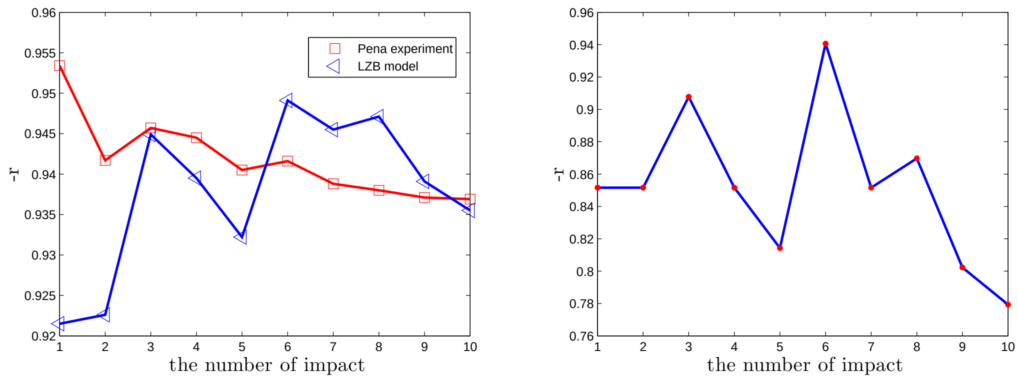

(a) From the estimation process.

(b) From $\frac{\dot{\theta}(t^+)}{\dot{\theta}(t^-)}$

Figure 10: Numerical and experimental values of the angular restitution coefficient (specimen 1 with fitted parameters).

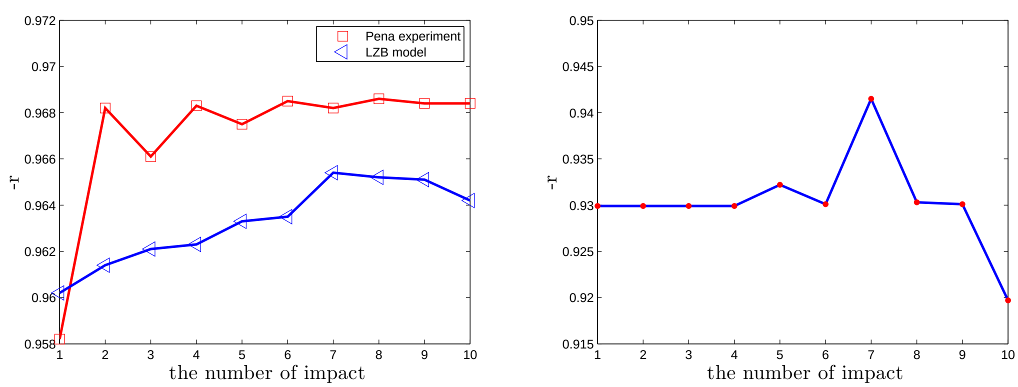

(a) From the estimation process.

(b) From $\frac{\dot{\theta}(t^+)}{\dot{\theta}(t^-)}$

Figure 11: Numerical and experimental values of the angular restitution coefficient (specimen 2 with fitted parameters).

- (ii) The decrease of the fitted value for e_n^* for specimen 1 may be explained by some damage that has occurred on the contact points after the tenth impact ($t \approx 2.7$s), implying more dissipation. Indeed it is indicated in section 7 of [19, 20] that specimen 1 was damaged after the first tests. Since these experimental data are not ours we are unable to more accurately determine the source of this necessary variation of e_n^*. A similar process of decreasing/increasing the fitted value of e_n^* has been necessary for specimen 4 in figure 7, which is of the slice type. It is possible that the line contact assumption is not perfectly satisfied experimentally due to the large thickness, or due to the base geometry with large cuts (see figure 1 in [20]). Only a study on the impact force shape on the contact surface could bring an answer, but this is outside the scope of this study. Let us point out that no simulation result about specimen 4 is presented in [20], where it is mentioned that during the experiments specimen 4 shows small rotation around the vertical axis (that is a three-dimensional effect we cannot incorporate into our planar model). Other arguments concerning the two-point contact assumption, the line contact effects and the effective width are discussed in [19]. This may explain why we had to switch twice e_n^* to get good matching.

- (iii) The results in figures 9 are important because they directly relate to the uncertainty on the values of the width L (equivalently $\frac{l}{L}$) that may occur due to impact line or surface effects. These effects are in turn linked to the definition of the distance between the block and the ground, *i.e.* to the definition of the unilateral constraints, which are an essential ingredient in such a rigid body approach.

- (iv) When the block collides the ground at A while rotating around B, it may experience a sequence of small bounces at this corner A while performing a rocking motion. We call this phenomenon the rebound phase. Rebound phases are clearly seen in figures 5 (a) and 5 (b). It is somewhat surprizing that there may be rocking without 2-impacts, if the rebound phases do not vanish before the impact at the other corner, like in figures 5 (a) and 5 (b). In such cases one should speak of a macroscopic rocking motion, see figures 23 to 26 in [36].

- (v) It has been shown in [20] that specimen 3 that is of the tower-block type is prone to significant three dimensional effects like torsional effects and friction at the base. This explains why our planar model could not satisfactorily reproduce the experimental $\theta(t)$ response (figures 6 (a) and 6 (b)).

- (vi) The fact that r is constant during the rocking motion means that a kinematic law like the one in entry (3,3) in Table 1 in [6] can be used, provided that $e_{n,21}(= -r)$ can be chosen within the required interval. However an important part of the dynamics like the rebound phases after the first impact, may be missed in many instances of slender blocks. We infer that this kinematic law does represent the rocking motion only when there is perfect sticking at impacts and outside impacts, and when the rebound phases vanish (such cases exist, see [12] with $\frac{l}{L} = 8$). We reiterate also that such a law does not permit to *predict* that such a particular motion will occur, it can just be fitted *a posteriori*. If, anyway, one knows in advance that perfect rocking with sticking (or almost sticking) contact/impact points is going to occur, then a kinematic law may be preferred because of its simplicity that may be important for calculations.

Remark 3. *Simulations with the discrete element method (DEM) are presented in [19]. They seem at first sight to provide results of the same quality as ours. We should note however that the DEM involves more parameters than the LZB/complementarity one, and that there is a significant difference between the theoretical parameters (computed from the materials properties) and the fitted ones in [19], see Table III in [19]. Moreover it seems that there is no logic behind this process since the theoretical parameters may be larger or smaller than the fitted ones. For instance the ratio between the theoretical and fitted stiffness constants K for specimen 2 is equal to* $\frac{3302}{3449} \approx 0.957$ *while for specimen 1 it is* $\frac{7233}{6560} \approx 1.10$ *in Table III [19]. More generally it is clear that much* *more work is needed to compare the LZB/complementarity and the DEM approaches, particularly in terms of computational intensity, ease of parameter-fitting process, ability to apply to higher degree-of-freedom systems, three-dimensional blocks,* etc.

3.2 Comparisons with the experimental data of Lipscombe et al [12]

Other experimental data obtained with steel blocks/steel foundation are reported in [12], for $\frac{l}{L} = 1$ (specimen 1), 2 (specimen 2), 4 (specimen 3) and 8 (specimen 4). Figures 5, 6 and 7 in [12] show that "macroscopic" rocking occurs for $\frac{l}{L} = 2, 4$ and 8. However "perfect" rocking where the contact points stick after the shock, is obtained only for $\frac{l}{L} = 8$. For the other two values, the system becomes airborne after the first impact at B, then undergoes several impacts at B while still airborne. For $\frac{l}{L} = 4$ this sequence of impacts at B while airborne becomes much smaller, then disappears for $\frac{l}{L} = 8$. From a qualitative point of view, this indicates that perfect rocking occurs only for large enough $\frac{l}{L}$. This also confirms that the impact phases which are visible for instance in figures 5 (a) and 5 (b) do exist experimentally. Thanks to the small size of the blocks, values of $e^*_{n,i}$ have been measured and found to be close to 0.9 in [12]. However these values were measured in figure 11 of [12] for relative approach velocities within $[0.1, 0.4]$ m/s, which may be too large values for rocking motions, especially when the energy has dissipated sufficiently. Thus we have to fit e^*_n once again. The fitted values are $e^*_n = 0.5$ for specimen 1, $e^*_n = 0.9$ for specimen 2, $e^*_n = 0.98$ for specimens 3 and 4. The numerical results are depicted in figures 12 (a) (b), 12 (c) (d), 13 (a) and 13 (c). The friction coefficients are chosen as in [12] as $\mu = 0.16$ and $\mu_s = 1.3$ for the first three blocks, and $\mu = 0.13$ and $\mu_s = 0.28$ for the most slender block. The dashed curves in figures 12 (b), 13(c) and 13 (d) correspond to the simulations made in [12] with the so-called SRM (Simple Rocking Model). The SRM uses the Housner's angular velocity coefficient of restitution with angular momentum conservation. Some comments arise:

- The qualitative behaviour of the four blocks dynamics is well reproduced:
  - Specimen 1 does not rock but performs half-rocking (*i.e.* one corner sticks on the ground while the other one bounces repeatedly) with two impacts before coming to rest, see figure 12 (a) (b). This is the only example of flat block we were able to find in the literature, with experimental data.
  - The rebounds phase occurs during the whole motion for specimen 1, then its duration decreases for specimens 2 and 3 until it vanishes for specimen 4, see figures 12 (c) (d), 13 (a) (b) and 13 (c) (d).
  - The impacts during the rebounds phases are well reproduced. For specimen 1 there is a first impact at B followed by rebound of B, then A detaches also from the ground and the block is airborne during a certain time. Then a series of impacts at B occurs again before complete rest (figures 12 (a) (b)). For specimen 2 the impacts at B are equally distributed during the rocking phase (figures 12 (c) and 12 (d)). For specimen 3 the rebound phase at B becomes shorter with more impacts concentrated on the right of the first impact time (figures 13 (a) (b)). For specimen 4 the rebound phases reduces to the first impact at B (figures 13 (c) (d)).
  - The possibility of predicting airborne phases is quite important in many applications and is one source of strong limitation of the basic Housner's approach with angular velocity restitution [33].
- The fitted values for e^*_n are in agreement with the experimental values provided in [12] which are close to 0.9, except for specimen 1 where a large discrepancy exists.
- Due to the lack of accuracy on the data provided in the upper parts of figures 5, 6, 7 in [12] which concern the long term $\theta(t)$ responses, it was impossible to get a matching between

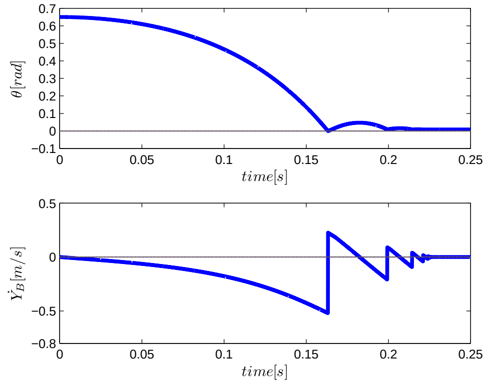

(a) simulation, $e^*_{n,i} = 0.5$, $l = 0.0458$m, $L = 0.0458$m.

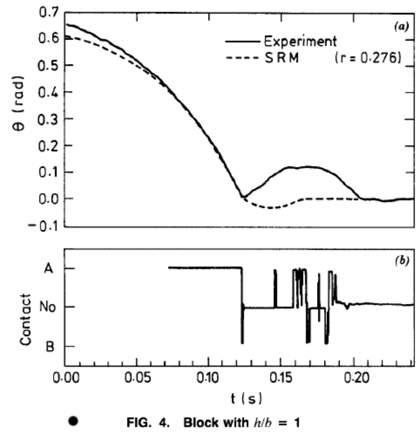

(b) figure 4 in [12].

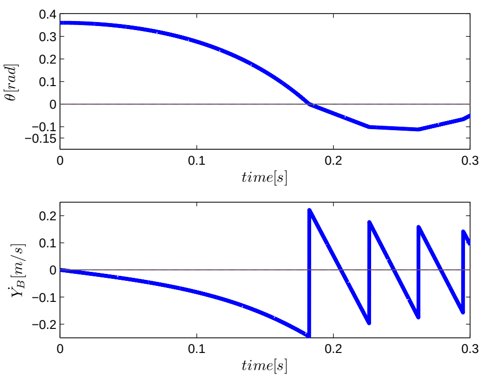

(c) simulation, $e^*_{n,i} = 0.9$, $l = 0.0916$m, $L = 0.0458$m.

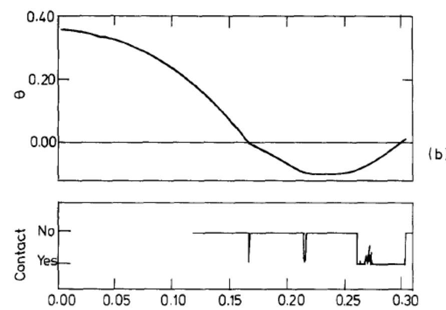

(d) figure 5 in [12].

Figure 12: Responses for: (a) (b) specimen 1, $\frac{l}{L} = 1$; (c) (d) specimen 2, $\frac{l}{L} = 2$.

numerical and experimental data as good as the one in section 3.1 for the evolution of $\theta(t)$ over a long period. Consider for instance the upper figure 7 of [12]. An initial angle $\theta(0) \approx 0.125$ rad is depicted, however this is larger than the critical angle α calculated from the dimensions which are given on page 1391 of [12]. There is consequently a strong mismatch between the data and the presented experimental results in that paper, which we cannot understand without having access to more informations. To be more concrete, we have even been unable to correctly simulate the block's motion before the first impact for specimens 2, 3 and 4 which rock, despite the dynamics on this period is simply that of an inverted pendulum. So the subsequent $\theta(t)$ responses were nonsense. The same is for the upper part of figure 6 in [12]. The simulations reported in [12] are not initialized as the experimental system, indicating that there may have been significant uncertainties during the experiments. The fact that we are able to qualitatively reproduce important phenomena is to be considered as the best results we could get.

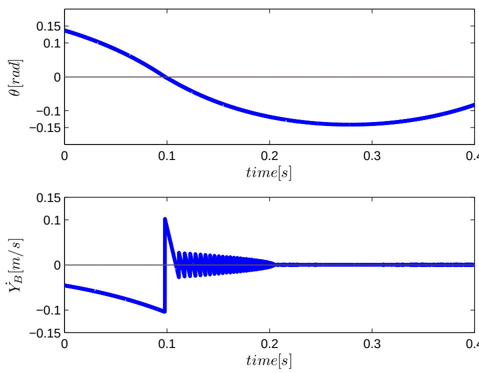

(a) simulation, $e^*_{n,i} = 0.98$, $l = 0.2032$m, $L = 0.0508$m.

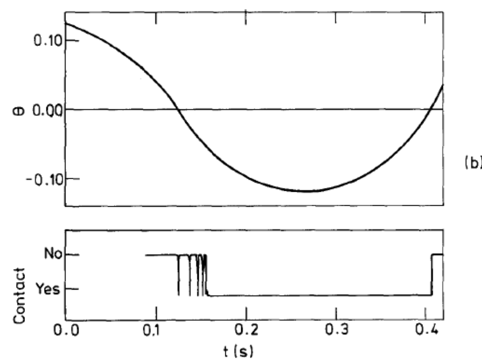

(b) figure 6 in [12].

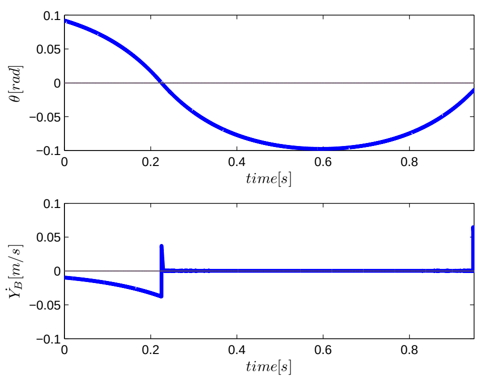

(c) simulation, $e^*_{n,i} = 0.98$, $l = 0.4064$m, $L = 0.0508$m.

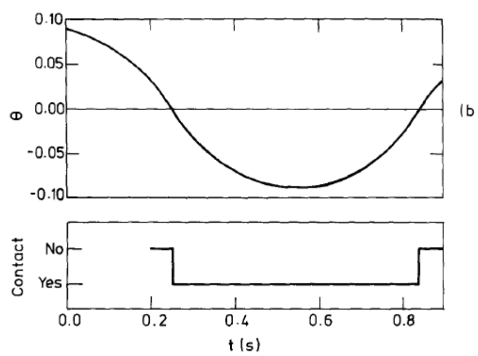

(d) figure 7 in [12].

Figure 13: Responses for: (a) (b) specimen 3, $\frac{l}{L} = 4$; (c) (d) specimen 4, $\frac{l}{L} = 8$.

4 Conclusions

Part I of this paper has focused on the experimental validation of the multiple impact law with Coulomb friction introduced in [13, 14, 15, 16, 39]. This impact law is based on the Darboux-Keller assumptions, and is a rigid body model incorporating flexibility effects, with few parameters *per contact* (restitution and friction coefficients). It is shown that this impact model, coupled to a complementarity model of the block outside the impacts, is able to reproduce successfully the free-rocking (fixed base). Detailed comparisons between the numerical results obtained with an event-driven method and the experimental data found in [12, 19, 20] are made (see also [36] for comparisons with the data in [8]). These comparisons prove that the model we use is able to correctly predict the free-rocking motion of various types of block/ground systems. Most importantly it is shown that the free-rocking data can be used to fit the impact law parameters. To the best of the authors' knowledge it is the first time that such an extensive simulation/experiments comparison work is performed, with data obtained independently by other authors. The obtained fitted parameters are then used for the more complex cases with base excitation in Part II. The future works should concern the analysis of the three-dimensional block (with four contact/impact points) and of stacked blocks. Incorporating lumped flexibilities in the structure, asymmetry in the block's geometry, irregular bases with more than two contact points, more complex base excitations, could also be beneficial.

Ackowledgements: the authors are very grateful to Dr Fernando Pena (UNAM Mexico) for providing them with detailed figures from the experiments in [20]. These data have been valuable for achieving this work. This work was performed with the support of the NSFC/ANR project Multiple Impact, ANR-08-BLAN-0321-01.

References

[1] V. Acary, B. Brogliato, *Numerical Simulation for Nonsmooth Dynamical Systems*, Springer Verlag Heidelberg, Lecture Notes in Applied and Computational Mechanics, vol.35, 2008.

[2] U. Andreaus, P. Casini, "Dynamics of three-block assemblies with unilateral deformable contacts. Part 1: contact modelling", Earthquake Engineering and Structural Dynamics, vol.28, pp.1621-1636, 1999.

[3] M. Aslam, W.G. Godden, D.T. Scalise, "Earthquake rocking response of rigid bodies", J. Struct. Engrg. ASCE, vol.106, no 2, pp.377-392, 1980.

[4] R. Boroschek, A. Iruretagoyena, "Controlled overturning of unanchored rigid bodies", Earthquake Engineering and Structural Dynamics, vol.35, no 6, pp.695-711, 2006.

[5] B. Brogliato, *Nonsmooth Mechanics*, Springer London, 2nd Ed., 1999.

[6] B. Brogliato, H. Zhang, C. Liu, "The planar rocking-block: analysis of kinematic restitution laws", submitted.

[7] S. Djerassi, "Collision with friction; Part A: Newton's hypothesis", Multibody Systems Dynamics, vol.29, pp.37-54, 2009.

[8] M.A. ElGawady, Q. Ma, J. W. Butterworth, J. Ingham, "Effects of interface material on the performance of free rocking blocks", Earthquake Engineering and Structural Dynamics, vol.40, no 4, pp.375-392, April 2011.

[9] Ch. Glocker, "Concepts for modeling impacts without friction", Acta Mechanica, vol.168, pp.1-19, 2004.

[10] G.W. Housner, "The behaviour of inverted pendulum structures during earthquakes", Bulletin of the Seismological Society of America, vol.53, no 2, pp.403-417, 1963.

[11] B. Imre, S. Rabsamen, S.M. Springman, "A coefficient of restitution of rock materials", Computers and Geosciences, vol.37, pp.339-350, 2008.

[12] P.R. Lipscombe, S. Pellegrino, "Free rocking of prismatic blocks", Journal of Engineering Mechanics, vol.119, no 7, pp.1387-1410, July 1993.

[13] C. Liu, Z. Zhao, B. Brogliato, 2008 "Frictionless multiple impacts in multibody systems: Part I. Theoretical framework", Proceedings of the Royal Society A, Mathematical, Physical and Engineering Sciences, vol.464, no 2100, pp.3193-3211, December.

[14] C. Liu, Z. Zhao, B. Brogliato, 2008 "Energy dissipation and dispersion effects in a granular media", Physical Review E, vol.78, no 3, 031307, September.

[15] C. Liu, Z. Zhao, B. Brogliato, 2008 "Variable structure dynamics in a bouncing dimer", INRIA Research Report 6718, November, http://hal.inria.fr/inria-00337482/fr/ .

[16] C. Liu, Z. Zhao, B. Brogliato, 2009 "Frictionless multiple impacts in multibody systems: Part II. Numerical algorithm and simulation results", Proceedings of the Royal Society A, Mathematical, Physical and Engineering Sciences, vol.465, no 2101, pp.1-23, January.

[17] H. Mouzakis, I. Psycharis, D. Papastamadiou, P. Carydis, C. Papantonopoulos, C. Zamba, "Experimental investigation of the earthquake response of a model of a marble classical column", Earthquake Engineering and Structural Dynamics, vol.31, pp.1681-1698, 2002.

[18] A. Palmeri, N. Makris, "Response analysis of rigid structures rocking on viscoelastic foundation", Earthquake Engineering and Structural Dynamics, vol.37, pp.1039-1063, 2008.

[19] F. Pena, F. Prieto, P.B. Lourenço, A. Campos Costa, J.V. Lemos, "On the dynamics of rocking motion of single rigid-block structures", Earthquake Engineering and Structural Dynamics, vol.36, pp.2383-2399, 2007.

[20] F. Pena, P.B. Lourenço, A. Campos-Costa, "Experimental dynamic behavior of free-standing multi-block structures under seismic loadings", Journal of Earthquake Engineering, vol.12, pp.953-979, 2008.

[21] M.J.N. Priestley, R.J. Evenson, A.J. Carr, "Seismic response analysis of structures free to rock on their foundations", Bull. of the New Zealand Seis. Soc. for Earthquake Engrg., vol.11, no 3, pp.141-150, 1978.

[22] F. Prieto, P.B. Lourenço, "On the rocking behavior of rigid objects", Meccanica, vol.40, pp.121-133, 2005.

[23] F. Prieto, P.B. Lourenço, C.S. Oliveira, "Impulsive Dirac-delta forces in the rocking motion", Earthquake Engineering and Structural Dynamics, vol.33, pp.839-857, 2004.

[24] M.D. Purvance, A. Anooshehpoor, J.N. Brune, "Freestanding block overturning fragilities: Numerical simulation and experimental validation", Earthquake Engineering and Structural Dynamics, vol.37, pp.791-808, 2008.

[25] H.W. Shenton, "Criteria for initiation of slide, rock, and slide-rock rigid-body modes", J. Eng. Mech. ASCE, vol.122, no 7, pp.690-693, 1996.

[26] B. Shi, A. Anooshenhpoor, Y. Zeng, J.N. Brune, "Rocking and overturning of precariously balanced rocks by earthquakes", Bulletin of the Seismological Society of America, vol.86, no 5, pp.1364-1371, October 1996.

[27] P.D. Spanos, A.S. Koh, "Rocking of rigid blocks during harmonic shaking", J. Engrg. Mech., vol.110, no 11, pp.1627-1642, 1984.

[28] A.B. Stevens, C.M. Hrenya, "Comparison of soft-sphere models to measurements of collision properties during normal impacts", Powder Technology, vol.154, pp.99-109, 2005.

[29] W.J. Stronge, *Impact Mechanics*, Cambridge University Press, 2000.

[30] T. Taniguchi, "Non-linear response analyses of rectangular rigid bodies subjected to horizontal and vertical ground motion", Earthquake Engineering and Structural Dynamics, vol.31, pp;1481-1500, 2002.

[31] W.K. Tso, C.M. Wong, "Steady state rocking response of rigid blocks. Part 1: Analysis", Earthquake Engineering and Structural Dynamics, vol.18, no 1, pp.89-106, 1989.

[32] W.K. Tso, C.M. Wong, "Steady state rocking response of rigid blocks. Part 2: Experiment", Earthquake Engineering and Structural Dynamics, vol.18, no 1, pp.107-120, 1989.

[33] T. Winkler, K. Meguro, F. Yamazaki, "Response of rigid body assemblies to dynamic excitation", Earthquake Engineering and Structural Dynamics, vol.24, pp.1389-1408, 1995.

[34] C. Yilmaz, M. Gharib, Y. Hurmuzlu, "Solving frictionless rocking block problem with multiple impacts", Proc. R. Soc. A, vol.465, pp.3323–3339, 2009.

[35] C.S. Yim, A.K. Chopra, J. Penzien, "Rocking response of rigid blocks to earthquakes", Earthquake Engineering and Structural Dynamics, vol.8, no 6, pp.565-587,1980.

[36] H. Zhang, B. Brogliato, "The planar rocking block: analysis of kinematic restitution laws, and a new rigid-body impact model with friction", INRIA Research Report RR-7580, March 2011, http://hal.inria.fr/inria-00579231/en/.

[37] H. Zhang, B. Brogliato, C. Liu, "Study of the planar rocking-block dynamics without and with friction: critical kinetic angles", submitted.

[38] H. Zhang, B. Brogliato, C. Liu, "Comparisons between numerical and experimental data for the planar rocking-block dynamics – Part II: analysis of the onset of rocking and of overturning", submitted.

[39] Z. Zhao, C. Liu, B. Brogliato, 2009 "Planar dynamics of a rigid body system with frictional impacts. II. Qualitative analysis and numerical simulations", Proceedings of the Royal Society A, Mathematical, Physical and Engineering Sciences, vol.465, no 2107, pp. 2267-2292, July.